

## Structural response of stainless steel oval hollow section compression members

M. Theofanous<sup>a,\*</sup>, T.M. Chan<sup>b</sup>, L. Gardner<sup>a</sup>

<sup>a</sup> Department of Civil and Environmental Engineering, Imperial College London, London SW7 2AZ, UK

<sup>b</sup> Civil and Mechanical Division, School of Engineering, University of Warwick, Coventry CV4 7AL, UK

### ARTICLE INFO

#### Article history:

Received 18 March 2008

Received in revised form

27 August 2008

Accepted 1 December 2008

Available online 15 January 2009

#### Keywords:

Column

Cross-section

Elliptical

Experiments

Finite element

Hollow section

Numerical modelling

Oval

Stainless steel

Stub column

Testing

Tubular construction

### ABSTRACT

Cold-formed stainless steel oval hollow sections (OHS) offer the combined aesthetic appeal of circular hollow sections and stainless steel, together with the structural efficiency associated with cross-sections of differing geometric properties about their two principal axes. To date, no structural design guidance exists for these cross-sections, principally due to their relatively recent introduction and a lack of fundamental structural test data. This paper examines the structural response of stainless steel OHS compression members and presents design recommendations. A series of laboratory tests was carried out to generate fundamental structural performance data. Tensile coupon tests were initially performed to establish the basic material stress-strain characteristics of the sections. These were followed by stub column tests to determine the average compressive response of the cross-sections and flexural buckling tests to obtain ultimate load carrying capacity data for use in the determination of a suitable buckling curve for stainless steel OHS. Measurements of the geometric properties of the test specimens including initial imperfections were carried out. The full load-displacement responses of the specimens were recorded and have been presented herein. A finite element (FE) modelling programme was performed in parallel with the experimental study. Once the FE models had been validated against the test results, parametric studies were carried out to further investigate the influence of individual key parameters, including the aspect ratio and local slenderness of the cross-sections as well as the member slenderness. Based on the obtained experimental and numerical results, a class 3 limit for stainless steel OHS in compression and a suitable buckling curve for OHS columns have been proposed.

© 2008 Elsevier Ltd. All rights reserved.

## 1. Introduction

The physical characteristics of stainless steel makes it well suited to use in construction; it possesses high strength and stiffness (comparable with carbon steel), very high ductility (approximately two times that of carbon steel), and excellent corrosion resistance, which means, suitably specified that it requires no protective coatings [1]. Stainless steel also offers better retention of strength and stiffness than carbon steel at elevated temperatures [2,3]. The principal disincentive for the application of stainless steel in construction is the initial material cost, though considered on a whole life basis, cost comparisons with carbon steel become more favourable. Structural design guidance is available for stainless steel in Eurocode 3: Part 1.4 [4]; the design rules are harmonised, where possible, with those developed for structural carbon steel in Eurocode 3: Part 1.1 [5], thus enabling relatively straightforward transition between the two materials. Stainless steel exhibits a rounded stress-strain

curve (see Fig. 1), which necessitates the use of a proof stress (generally the 0.2% proof stress) in place of a yield stress in the calculation of structural resistance, and use of the secant modulus in serviceability calculations. Strain hardening under load is also significant though the resulting enhancement in structural resistance is not currently incorporated in design codes. A method for harnessing this increase in resistance has been developed [6,7].

Exploiting its corrosion resistance and aesthetic appeal, stainless steel is often employed for exposed structural elements, a number of examples of which are given in [8]. Tubular construction is also becoming increasingly popular for such applications. Until recently, the primary tubular cross-section shapes available to structural engineers and architects have been square, rectangular and circular. Now, hot-rolled carbon steel elliptical hollow sections (EHS) and cold-formed stainless steel oval hollow sections (OHS) are available for structural applications. These sections offer the architectural attributes of circular hollow sections, together with the structural advantages associated with sections of differing properties about the two principal axes. This paper focuses on the structural response of cold-formed stainless steel oval hollow section compression members, though comparisons are made with the results from previous studies on carbon steel elliptical hollow sections [9–11].

\* Corresponding author. Tel.: +44 0 207 594 6031.

E-mail addresses: [marios.theofanous@imperial.ac.uk](mailto:marios.theofanous@imperial.ac.uk) (M. Theofanous), [T.M.Chan@warwick.ac.uk](mailto:T.M.Chan@warwick.ac.uk) (T.M. Chan), [leroy.gardner@imperial.ac.uk](mailto:leroy.gardner@imperial.ac.uk) (L. Gardner).

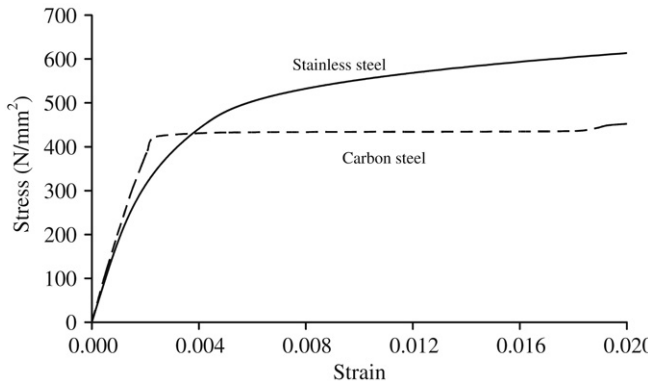


**Fig. 1.** Indicative stainless steel and carbon steel material stress–strain behaviour.

## 2. Experimental studies

### 2.1. Introduction

A series of tensile material tests, compressive stub column tests and flexural buckling tests were carried out to investigate the structural behaviour of stainless steel oval hollow section compression members. All tests were performed in the Structures laboratory of the Department of Civil and Environmental Engineering at Imperial College London. Three section sizes were employed for the stub column tests—OHS 121 × 76 × 2, OHS 121 × 76 × 3 and OHS 86 × 58 × 3, whilst all flexural buckling tests were conducted on OHS 86 × 58 × 3. All tested material was austenitic stainless steel, grade 1.4401 (316), which contains approximately 18% chromium and 10% nickel [12]. All specimens were cold-rolled and seam welded. The minimum specified yield strength (0.2% proof strength) for grade 1.4401 stainless steel is 240 N/mm<sup>2</sup> for cold-rolled sheet material (up to 8 mm in thickness) and 220 N/mm<sup>2</sup> for hot-rolled sheet material (up to 13.5 mm in thickness) [13]. However, the material strength of stainless steel is considerably enhanced during the sheet and section forming processes due to cold-working, as indicated by previous test results [14–17] and verified in the present study. This section summarises the testing apparatus, the experimental procedures and the test results obtained.

### 2.2. Tensile coupon tests

Tensile coupon tests were performed to establish the basic material stress–strain response; this was subsequently utilised during the analysis of the member test results and in the development of numerical models. The tests were carried out in accordance with EN 10002-1 (2001) [18].

Parallel coupons were machined longitudinally from the two flattest portions of the cross-sections (i.e. along the centrelines of the minor axis) using a tipped slot-drill. Longitudinal curving of the coupons was observed as machining progressed, indicating the presence of through-thickness residual stresses. However, no attempt was made to straighten the coupons (by plastic bending) prior to tensile testing. The nominal dimensions of the tensile coupons were 350 × 20 mm. Holes were drilled and reamed 20 mm from each end of the coupons for pins to be inserted to prevent slippage of the coupons in the jaws of the testing machine. Proportional gauge lengths [18] were marked along the coupons to calculate the strain at fracture. A summary of the mean measured dimensions for the tensile coupons are given in Table 1. Two coupon tests, designated TC1 and TC2, were performed for each section size.

Linear electrical strain gauges were affixed at the midpoint of each side of the tensile coupons. Load, strain, displacement



**Fig. 2.** Stub column testing apparatus.

and input voltage were all recorded using the data acquisition equipment DATASCAN and logged using the DALITE computer package. All data were recorded at one second intervals. The tensile tests were performed using an Amsler 100 kN hydraulic testing machine. Strain rates were within the limits prescribed by EN 10002-1 [18].

The key results from the six coupon tests are summarised in Table 2, where  $E_0$  is the initial tangent modulus,  $\sigma_{0.2}$  and  $\sigma_{1.0}$  are the 0.2% and 1% proof strengths respectively,  $\sigma_u$  is the ultimate tensile strength,  $\varepsilon_f$  is the plastic strain at fracture and  $n$  and  $n_{0.2,1.0}$  are strain hardening exponents for the compound Ramberg–Osgood model described in [7]. The adopted compound model was developed on the basis on a two-stage version [19,20] of the original Ramberg–Osgood expression [21,22].

### 2.3. Stub column tests

A total of six stainless steel oval hollow section (OHS) stub columns were tested in pure axial compression to assess load carrying capacity and deformation capacity and enable the determination of a suitable Class 3 limit for stainless steel OHS in compression. Full load–end shortening curves were recorded, including into the post-ultimate range.

The specimens were cut roughly to length using a rotary hacksaw. Their ends were milled flat and square to a tolerance of ±0.02 mm to achieve accurate seating in the testing machine. Prior to testing, strain visualisation grids were marked onto the surface of the specimens, and measurements of geometry, including initial imperfections were taken. The nominal lengths of the stub columns were chosen such that they were sufficiently short not to fail by overall buckling, yet still long enough to contain representative distributions of residual stresses and geometric imperfections. The stub column lengths were taken as two times the larger cross-sectional dimension.

The stub column tests were carried out in a self-contained 300 T Amsler hydraulic testing machine (Fig. 2). The tests were load-controlled through an Amsler control cabinet. The end platens of the testing apparatus were fixed flat and parallel. Alignment of

**Table 1**

Mean measured dimensions of tensile coupons.

Coupon designation	Width $b$ (mm)	Thickness $t$ (mm)	Cross-sectional area $A$ (mm $^2$ )	Original gauge length (mm)
OHS 121 × 76 × 2-TC1	19.21	1.82	34.97	32.0
OHS 121 × 76 × 2-TC2	19.19	1.83	35.14	32.0
OHS 121 × 76 × 3-TC1	19.97	3.00	59.93	42.0
OHS 121 × 76 × 3-TC2	20.02	2.98	59.58	42.0
OHS 86 × 58 × 3-TC1	20.02	3.15	63.00	44.0
OHS 86 × 58 × 3-TC2	19.98	3.13	62.59	44.0

**Table 2**

Measured material properties from tensile coupons.

Coupon designation	$E_0$ (N/mm $^2$ )	$\sigma_{0.2}$ (N/mm $^2$ )	$\sigma_{1.0}$ (N/mm $^2$ )	$\sigma_u$ (N/mm $^2$ )	$\varepsilon_f$	Modified R-O coefficients	
						$n$	$n'_{0,2,1,0}$
OHS 121 × 76 × 2-TC1	193 900	380	426	676	0.61	7.8	2.9
OHS 121 × 76 × 2-TC2	193 300	377	419	672	0.60	8.9	2.9
OHS 121 × 76 × 3-TC1	194 100	420	460	578	0.58	9.7	4.0
OHS 121 × 76 × 3-TC2	190 400	428	467	583	0.58	8.2	4.0
OHS 86 × 58 × 3-TC1	194 500	339	368	586	0.62	14.0	1.8
OHS 86 × 58 × 3-TC2	194 500	331	349	597	0.62	13.5	1.3

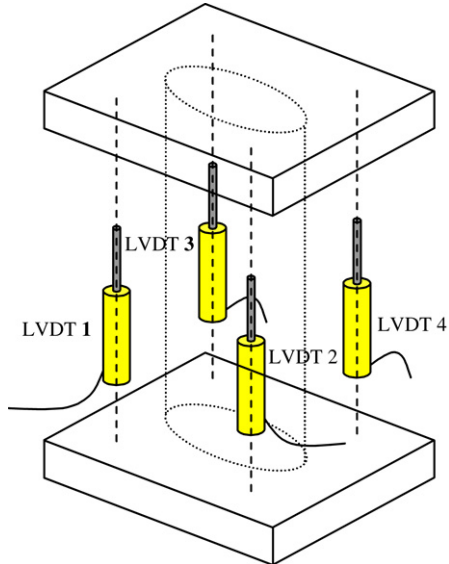


Fig. 3. Location of displacement transducers (LVDTs).

the specimens was necessary to ensure that the compressive load was introduced concentrically. This was carried out by applying a small alignment load to the specimens, approximately 10% of the predicted failure load  $F_{u,pred}$  and observing the variation in strain around the cross-section. In all cases the variation between strains at any point from the average strain was less than 5%. Linearity of the stress-strain plot was used to confirm that the alignment load was below the proportional limit.

Four linear variable displacement transducers (LVDTs) were used to determine the end shortening of the stub columns between the end platens of the testing machine. Fig. 3 shows a schematic view of their layout. Four linear electrical resistance strain gauges were affixed to each specimen at mid-height, and at a distance of four times the material thickness from the major axis. The strain gauges were initially used for alignment purposes, and later to modify the end shortening data from the LVDTs to eliminate the elastic deformation of the end platens [16]. Load, strain, displacement, and input voltage were all recorded at 2 s intervals.

Measurements of major and minor axis diameters, material thickness and stub column length were taken at four different points for each specimen. The mean measured dimensions for the six stub column specimens are presented in Table 3; cross-section geometry and notation is defined in Fig. 4. Two stub column tests,

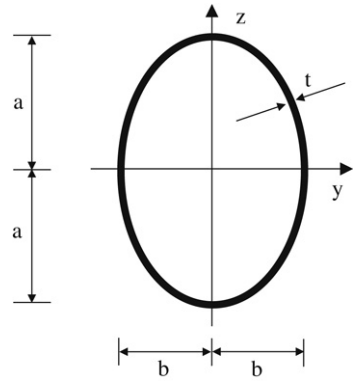


Fig. 4. Geometry and notation for oval hollow sections.

designated SC1 and SC2, were performed for each section size. The circumferences of the oval specimens were traced to determine their exact cross-sectional profiles. These were subsequently fitted with the equation of an ellipse, which was found to provide a suitably accurate representation of the geometry, an example of which is shown in Fig. 5. The cross-sectional area  $A$  of the test specimens was calculated as the circumference  $P_m$  (determined along the centreline of the thickness and calculated from Eq. (1) multiplied by the material thickness  $t$ , as recommended in [9].

$$P_m = \pi(a_m + b_m) \times (1 + 0.25h_m) \quad (1)$$

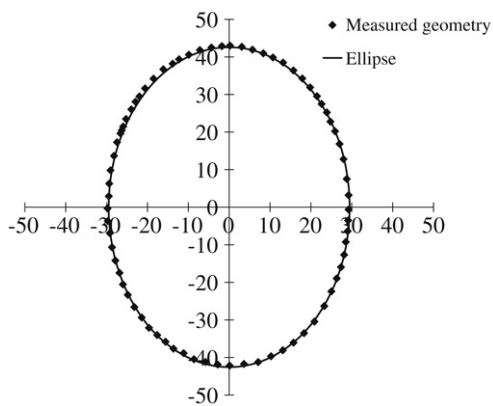
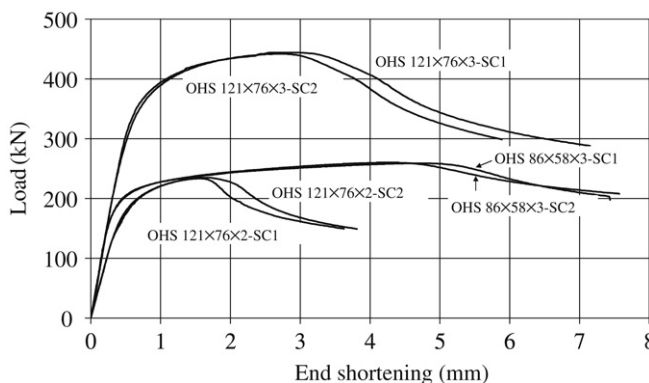
in which  $a_m = (2a - t)/2$ ,  $b_m = (2b - t)/2$  and  $h_m = (a_m - b_m)^2/(a_m + b_m)^2$ .

Measurements of local initial geometric imperfections are important in aiding the explanation of structural response and in the development of numerical models. Schafer and Peköz [23] conducted a detailed assessment of initial geometric imperfections in cold-formed channel sections. In their experimental set-up, the specimens were mounted on the table of a milling machine, and a displacement transducer, fitted in the head of the milling machine, was employed to trace the local geometric imperfections. A similar arrangement was adopted in [16] and in the present study. Readings were taken at 20 mm intervals along the centrelines of the minor and major axes of the specimens. The datum line for the imperfection measurements was initially taken as a straight line connecting the ends of each stub column face. However, it was observed that the release of residual stresses following cutting to length induced flaring at the ends of the stub columns. The resulting imperfection amplitudes  $w_0$  were therefore not

**Table 3**

Mean measured dimensions of stub columns.

Stub column designation	Larger outer diameter $2a$ (mm)	Smaller outer diameter $2b$ (mm)	Thickness $t$ (mm)	Cross-sectional area $A$ ( $\text{mm}^2$ )	Length $L$ (mm)	Imperfection amplitude $w_0$ (mm)	Imperfection amplitude $w_{0.5}$ (mm)
OHS 121 × 76 × 2-SC1	123.70	76.94	1.84	577.3	242.0	1.06	0.31
OHS 121 × 76 × 2-SC2	124.14	76.60	1.84	577.1	242.0	0.96	0.27
OHS 121 × 76 × 3-SC1	121.53	77.14	2.94	902.1	241.7	0.96	0.21
OHS 121 × 76 × 3-SC2	121.56	77.09	2.95	904.0	241.2	1.19	0.33
OHS 86 × 58 × 3-SC1	85.63	57.22	3.11	674.4	171.9	0.78	0.20
OHS 86 × 58 × 3-SC2	84.67	58.98	3.12	678.4	171.6	1.01	0.29

**Fig. 5.** Measured geometry of oval section and elliptical representation.**Fig. 6.** Load-end shortening curves for OHS stub columns.

representative of the general geometric imperfection distribution in specimens. The effect of the end flaring was therefore removed by considering only the middle 50% of the specimens' length in the definition of the datum line, as proposed in [24]. The imperfection amplitudes based on this modified datum line, henceforth  $w_{0.5}$ , are included in Table 3 together with  $w_0$ .

Measured end shortening readings from the LVDTs were modified on the basis of the strain gauge readings to account for the elastic deformation of the end platens (that are present in the LVDT measurements) [16]. Thus true end shortening values were derived, and are utilised in the remainder of this study. Load–end shortening curves from the six stub column tests are shown in Fig. 6, whilst a summary of the key test results including ultimate load  $F_u$  and end shortening at ultimate load  $\delta_u$  is given in Table 4. In general, the test results indicate good correlation between the repeated stub column tests (SC1 and SC2).

Compression tests on stub columns reveal the average compressive response of the cross-sections and include implicitly the effects of strain-hardening and residual stresses induced during the cold-forming process. The compound Ramberg–Osgood

model [7] has been used to capture the average compressive stress–strain response, as determined from the stub column tests, the resulting parameters for which are presented in Table 5.

Ultimate failure was due to local buckling of the cross-sections. All the stub columns exhibited a similar failure mode whereby the two flatter portions of the specimens (i.e. the regions of maximum radius of curvature) buckled locally. Photographs of the deformed specimens 121 × 76 × 2 are shown in Fig. 7.

#### 2.4. Flexural buckling tests

Flexural buckling tests about the major and minor axes were carried out in order to obtain ultimate load carrying capacity data to enable the determination of a suitable buckling curve for stainless steel oval hollow section columns. The tests were conducted on pin-ended columns with nominal cross-sectional dimensions of 86 × 58 × 3 mm. The buckling lengths considered ranged from 700 mm to 3100 mm; these lengths were chosen to cover a spectrum of member slendernesses, as defined by Eq. (2), ranging between 0.34 and 2.07.

$$\bar{\lambda} = \sqrt{A\sigma_{0.2}/N_{cr}} \quad (2)$$

where  $A$  is the cross-sectional area,  $\sigma_{0.2}$  is the material 0.2% proof strength as determined from tensile coupon tests and  $N_{cr}$  is the elastic buckling load of the column.

The specimens were cut to the required lengths by a rotary hacksaw and the ends were milled flat to ensure full contact with the end plates. Subsequently, measurements of specimen geometry and initial global imperfections  $e_0$  were taken and are presented in Table 6. The designations 'CMI' and 'CMA' refer to minor and major axis buckling respectively.

The tests were carried out in a 400 T capacity rig (Fig. 8). The load was applied through end plates that were attached to hardened steel knife-edges (Fig. 9) designed to replicate pinned end conditions. The buckling lengths reported in Table 6 were measured between the pinned ends of each column, i.e. between the knife edges. The columns were aligned such that the centrelines of the cross-sections coincided with the middle of the knife edges, though, as discussed later, an unintentional eccentricity of approximately  $L/1250$  (complimentary to the initial global geometric imperfections) was also present in all tests.

Two displacements transducers were placed at the mid-height of the columns to measure the lateral deflection. Two further displacement transducers were placed on each of the end-plates to measure end rotations, while an additional two were employed to measure the end shortening. Four strain gauges were attached at a 50 mm distance from mid-height at each section's major and minor axis. Test data from the transducers, strain gauges, compressive load and the horizontal and vertical displacements were recorded at two second intervals. Key results from the column tests are summarised in Table 7 and load–lateral displacement at mid height curves are shown in Fig. 10 both for major and minor axis buckling columns.

As expected, all the columns failed principally by global buckling, with the maximum lateral displacement occurring at

**Table 4**

Summary of results from stub column tests.

Stub column designation	Ultimate load $F_u$ (kN)	End shortening at ultimate load $\delta_u$ (mm)
OHS 121 × 76 × 2-SC1	234	1.55
OHS 121 × 76 × 2-SC2	235	1.63
OHS 121 × 76 × 3-SC1	444	2.77
OHS 121 × 76 × 3-SC2	442	2.71
OHS 86 × 58 × 3-SC1	259	4.69
OHS 86 × 58 × 3-SC2	260	4.25

**Table 5**

Measured material properties from stub column tests.

Coupon designation	$E_0$ (N/mm <sup>2</sup> )	$\sigma_{0.2}$ (N/mm <sup>2</sup> )	$\sigma_{1.0}$ (N/mm <sup>2</sup> )	Modified R-O coefficients	
				$n$	$n'_{0.2,1.0}$
OHS 121 × 76 × 2-SC1	185 000	380	426	7.9	4.1
OHS 121 × 76 × 2-SC2	189 000	380	426	8.3	4.1
OHS 121 × 76 × 3-SC1	176 800	444	492	10.1	4.2
OHS 121 × 76 × 3-SC2	176 650	438	489	8.3	4.1
OHS 86 × 58 × 3-SC1	178 000	317	361	10.9	4.1
OHS 86 × 58 × 3-SC2	182 000	318	360	9.1	4.1

**Table 6**

Measured geometric properties of columns.

Specimen	Larger outer diameter $2a$ (mm)	Smaller outer diameter $2b$ (mm)	Thickness $t$ (mm)	Cross-sectional area $A$ (mm <sup>2</sup> )	Buckling length (mm)	Global imperfection amplitude $e_0$ (mm)
86 × 58 × 3-CMI1	85.41	57.16	3.11	672.7	699.5	0.08
86 × 58 × 3-CMA1	85.48	56.84	3.09	668.5	700.6	0.11
86 × 58 × 3-CMI2	86.05	56.21	3.11	672.9	1499.6	1.43
86 × 58 × 3-CMA2	85.91	56.70	3.15	681.4	1500.5	2.17
86 × 58 × 3-CM13	86.18	56.22	3.11	674.2	2299.3	2.78
86 × 58 × 3-CMI4	86.02	56.33	3.12	675.0	3100.3	1.73

**Table 7**

Key results from flexural buckling tests.

Specimen	Non-dimensional slenderness $\bar{\lambda}$	Ultimate load $N_u$ (kN)	Lateral deflection at $N_u$ (mm)
86 × 58 × 3-CMI1	0.46	181.8	9.5
86 × 58 × 3-CMA1	0.34	196.9	3.8
86 × 58 × 3-CMI2	1.00	116.1	17.8
86 × 58 × 3-CMA2	0.72	150.8	5.8
86 × 58 × 3-CM13	1.54	72.3	17.5
86 × 58 × 3-CMI4	2.07	40.6	29.9

mid-height. Upon detailed examination of the response of the tested specimens, it was observed that a small loading eccentricity with respect to the axis of buckling was introduced during testing—the value of this eccentricity was approximately  $L/1250$ , as estimated from the strain gauge data. This eccentricity has been included in subsequent numerical models. Typical column failure modes are shown in Fig. 11. The results of all tests are examined in Section 4 of this paper.

### 3. Numerical modelling

#### 3.1. Introduction

A numerical modelling programme was performed in parallel with the testing programme, using the non-linear finite element analysis package ABAQUS, Version 6.6 [25]. Two types of numerical analyses were performed for each model; linear elastic buckling analyses were initially carried out to determine buckling mode shapes, which were subsequently incorporated in geometrically and materially non-linear analyses as a representation of geometric imperfections. The modified Riks method [25] was employed for the non-linear analyses, which enabled the post-ultimate load response (i.e. the unload-

ing branch of the load–displacement curve) of the models to be captured.

Shell elements were adopted to simulate the stainless steel oval hollow section stub and long columns as is customary for the modelling of thin-walled structures. The ABAQUS element library [25] contains a range of shell elements, as discussed in [26]. The element employed in the present study is S4R, a 4-noded doubly curved general-purpose shell element, with reduced integration and finite membrane strains, which has performed well in numerous similar applications [27,28]. A mesh convergence study based on elastic eigenvalue buckling analyses was performed to choose a mesh size that would produce accurate results whilst remaining computationally efficient. A uniform mesh along the circumferential and longitudinal directions of size  $2a/10(a/b) \times 2a/10(a/b)$  (where  $a$  and  $b$  are defined in Fig. 4) was deemed suitable and was employed for both the stub column and long column models.

The initial aim of the numerical study was to replicate the experimental results and assess the sensitivity of the models to mesh density, material properties and initial geometric imperfections. Once validated, a series of parametric studies were carried out to investigate the influence of key variables (in particular cross-section slenderness and aspect ratio for the stub columns and global slenderness, aspect ratio and axis of buckling for the long columns) and generate further results.



**Fig. 7.** Deformed OHS 121 × 76 × 2 stub columns.



**Fig. 8.** Test setup for flexural buckling tests.

### 3.2. Numerical modelling of stub columns

Geometry, end restraints, loading and experimentally observed failure modes were symmetric about both the major and minor axes for all stub column tests. This symmetry was exploited in the FE simulations by modelling only one quarter of the cross-section and applying appropriate symmetry boundary conditions along the major and minor axes of the sections. Kinematic coupling was employed to constrain the vertical displacement of all nodes at the loaded end. The ends of the stub column models were fixed against all degrees of freedom except for the vertical displacement at the loaded edge in accordance with other numerical studies on stub columns [26,27]. However, it was later observed that the circumferential expansion of the

cross-sections due to the Poisson effect during the non-linear analyses effectively induced an additional geometric imperfection near the loaded ends of the models, which were not allowed to expand. This additional induced imperfection was found generally to be more significant than the critical geometric imperfection itself (incorporated by means of the lowest buckling mode shape) even for high imperfection amplitudes. The result of this was to induce an elephant's foot failure mode and a smooth post-ultimate response, which deviated from the experimental observations. Although the pre-buckling response prior reaching the ultimate load was relatively insensitive to the in-plane boundary conditions imposed on the ends of the model, the unloading response and failure mode was affected. Therefore, despite accurate predictions of the ultimate load still being possible with restrained ends, it was decided not to restrain the in-plane translations at the ends of the models in the non-linear analyses, to enable the entire load–displacement response and failure mode to be consistently and accurately be captured.

Measured geometric and material properties were used in each model to replicate the corresponding test behaviour. Both tensile coupon and stub column material properties were obtained during the experimental phase of this study (Tables 2 and 5) and were incorporated into the models. Hence, two series of numerical analyses were carried out; one utilizing tensile material properties and one utilizing stub column material properties. The material stress–strain parameters were averaged for each nominal cross-section size and applied uniformly around the cross-sections of the models in a multi-linear form. ABAQUS requires that the material properties are specified in terms of true stress  $\sigma_{true}$  and log plastic strain  $\varepsilon_{in}^{pl}$ , which may be derived from the nominal engineering stress–strain curves through Eqs. (3) and (4).

$$\sigma_{true} = \sigma_{nom}(1 + \varepsilon_{nom}) \quad (3)$$

$$\varepsilon_{in}^{pl} = \ln(1 + \varepsilon_{nom}) - \frac{\sigma_{true}}{E} \quad (4)$$

where  $\sigma_{nom}$  and  $\varepsilon_{nom}$  are engineering stress and strain respectively and  $E$  is the Young's modulus. The continuous  $\sigma_{nom}$ – $\varepsilon_{nom}$  curve was initially approximated with a multilinear curve which was subsequently converted into the required  $\sigma_{true}$ – $\varepsilon_{in}^{pl}$  format. The density of the points defining the multilinear curve was proportional to the curvature of the Ramberg–Osgood curve, in order to optimize the accuracy for a given number of points [29].

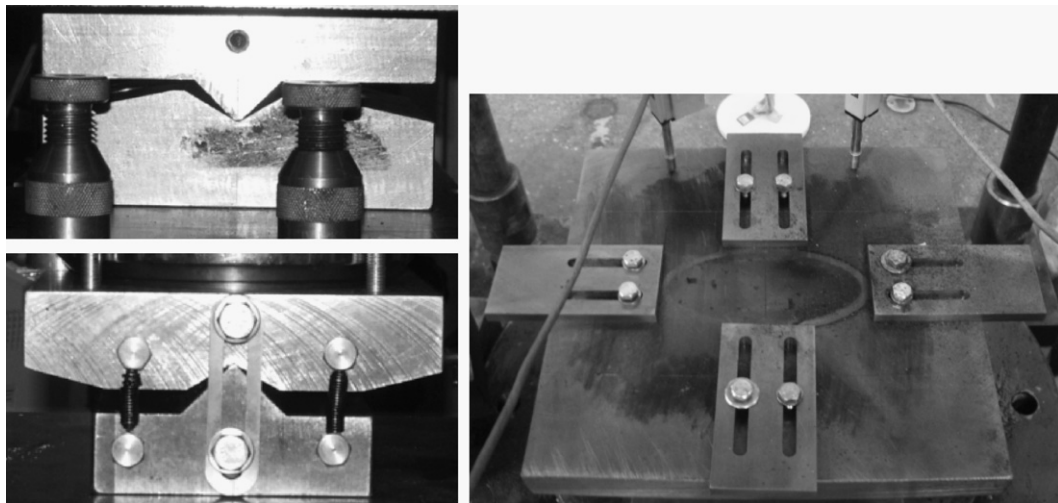


**Fig. 9.** Knife-edges and sliding clamps employed for the flexural buckling tests.

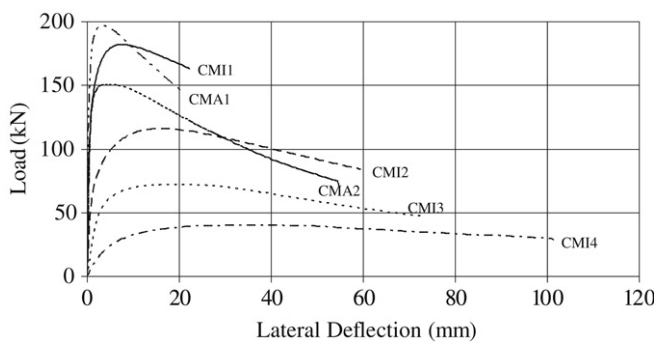


**Fig. 10.** Load–lateral displacement curves for OHS columns.

Residual stresses were not measured during the testing programme and were not included in the numerical models. However, as mentioned in Section 2.2 of this paper, the presence of through-thickness residual stresses was indicated by the longitudinal curving of the coupons as they were released from the cross-sections during machining. Such residual stresses have been observed previously [30,31] and it was concluded [26] that provided the coupons were not straightened (by plastic deformation) prior to testing, the residual stresses would be inherently present in the material stress-strain curve and did not therefore have to be explicitly included in numerical models. For membrane residual stresses (that may have been introduced due to differential cooling following seam welding of the oval sections), this would not be the case, though the influence of membrane residual stresses on similar structural components has been assessed in previous studies and found to be small [26,27].

Initial geometric imperfections are introduced into structural sections during production, fabrication and handling and can significantly influence structural behaviour. In this study, the imperfection shapes for the stub columns were taken as the lowest buckling modes obtained from a linear eigenvalue buckling analysis, a typical example of which is shown in Fig. 12. The amplitude of the imperfections was varied to assess the sensitivity of the models. Five imperfection amplitudes were considered: the maximum measured amplitudes from the testing programme  $w_0$  and  $w_{0.5}$  and three different fractions of the cross-sectional thickness  $t$  ( $t/10$ ,  $t/100$  and  $t/500$ ). Results and comparison with test behaviour for the five imperfection amplitudes are shown in Tables 8 and 9 for tensile and stub column material properties respectively.

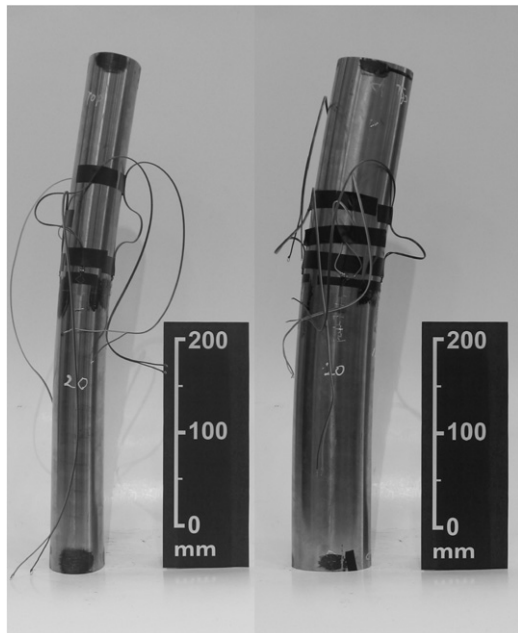


**Fig. 11.** Typical failure modes of OHS columns.

The response of the FE models was found to be sensitive to the amplitude of the geometric imperfection, as shown in Tables 8 and 9. It may also be seen that incorporation of the measured imperfection amplitude  $w_0$  (including flaring deformations at the ends of the stub columns) in the numerical models leads to a considerable underprediction of their load-carrying capacity. On the other hand, incorporation of the  $w_{0.5}$  imperfection amplitude (based on the central 50% of the stub columns' length) resulted in improved predictions of load-carrying capacity. Regarding the choice of material properties, it can be concluded that adoption of stub column material properties in the FE models yields more accurate results than incorporation of the tensile coupon properties. The improved accuracy resulting from the use of the stub column properties is believed to relate to basic differences in stress-strain curves in tension and compression and the inherent presence of the varying level of cold-work around the section in the stub column properties.

Overall, the FE models have been found to be capable of replicating the experimentally observed fundamental structural response characteristics of the stainless steel OHS stub columns.

**Table 8**

Comparison of stub column test results with FE results for varying imperfection amplitudes and tensile material properties.

Stub column designation	$w_0$		$w_{0.5}$		$t/10$		$t/100$		$t/500$	
	FE $F_u$ / Test $F_u$	FE $\delta_u$ / Test $\delta_u$	FE $F_u$ / Test $F_u$	FE $\delta_u$ / Test $\delta_u$	FE $F_u$ / Test $F_u$	FE $\delta_u$ / Test $\delta_u$	FE $F_u$ / Test $F_u$	FE $\delta_u$ / Test $\delta_u$	FE $F_u$ / Test $F_u$	FE $\delta_u$ / Test $\delta_u$
OHS 121 × 76 × 2-SC1	0.78	0.63	0.91	0.60	0.92	0.72	1.01	1.08	1.04	1.39
OHS 121 × 76 × 2-SC2	0.78	0.58	0.92	0.58	0.91	0.68	1.00	1.00	1.03	1.26
OHS 121 × 76 × 3-SC1	0.82	0.40	0.91	0.65	0.89	0.44	0.95	0.96	0.96	1.12
OHS 121 × 76 × 3-SC2	0.80	0.39	0.89	0.44	0.89	0.44	0.96	0.93	0.97	1.17
OHS 86 × 58 × 3-SC1	0.87	0.23	0.96	0.54	0.94	0.52	1.06	1.15	1.13	1.57
OHS 86 × 58 × 3-SC2	0.85	0.25	0.95	0.62	0.95	0.61	1.08	1.36	1.14	1.85
Mean	0.82	0.41	0.92	0.57	0.92	0.57	1.01	1.08	1.04	1.39
COV	0.04	0.40	0.03	0.13	0.03	0.21	0.05	0.15	0.07	0.20

**Table 9**

Comparison of stub column test results with FE results for varying imperfection amplitudes and stub column material properties.

Stub column designation	$w_0$		$w_{0.5}$		$t/10$		$t/100$		$t/500$	
	FE $F_u$ / Test $F_u$	FE $\delta_u$ / Test $\delta_u$	FE $F_u$ / Test $F_u$	FE $\delta_u$ / Test $\delta_u$	FE $F_u$ / Test $F_u$	FE $\delta_u$ / Test $\delta_u$	FE $F_u$ / Test $F_u$	FE $\delta_u$ / Test $\delta_u$	FE $F_u$ / Test $F_u$	FE $\delta_u$ / Test $\delta_u$
OHS 121 × 76 × 2-SC1	0.78	0.65	0.92	0.62	0.96	0.73	1.02	0.99	1.03	1.19
OHS 121 × 76 × 2-SC2	0.79	0.60	0.92	0.60	0.95	0.69	1.01	0.93	1.03	1.03
OHS 121 × 76 × 3-SC1	0.85	0.43	0.94	0.70	0.95	0.66	1.00	1.00	1.01	1.11
OHS 121 × 76 × 3-SC2	0.83	0.42	0.95	0.64	0.96	0.68	1.01	1.02	1.02	1.19
OHS 86 × 58 × 3-SC1	0.87	0.33	0.96	0.57	0.94	0.46	1.01	1.02	1.06	1.33
OHS 86 × 58 × 3-SC2	0.85	0.27	0.94	0.43	0.94	0.42	1.02	0.94	1.05	1.36
Mean	0.83	0.45	0.94	0.59	0.95	0.61	1.01	0.98	1.03	1.20
COV	0.04	0.33	0.02	0.16	0.01	0.22	0.01	0.04	0.02	0.10

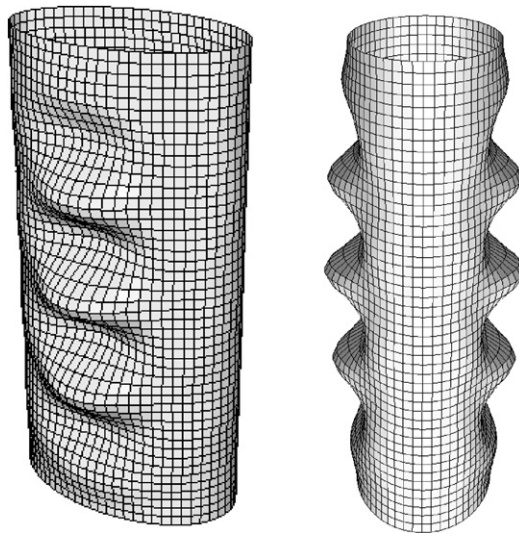


Fig. 12. Typical stub column lowest buckling mode shape.

The initial stiffnesses, peak loads, post-ultimate responses and failure modes of all modelled stub columns are generally well-predicted for both tensile and stub column properties. Excellent agreement with experimental results was obtained for an imperfection amplitude of  $t/100$  and using stub column material properties. The numerical load-displacement curves for OHS 121 × 76 × 3-SC1 and OHS 86 × 58 × 3-SC1 using stub column

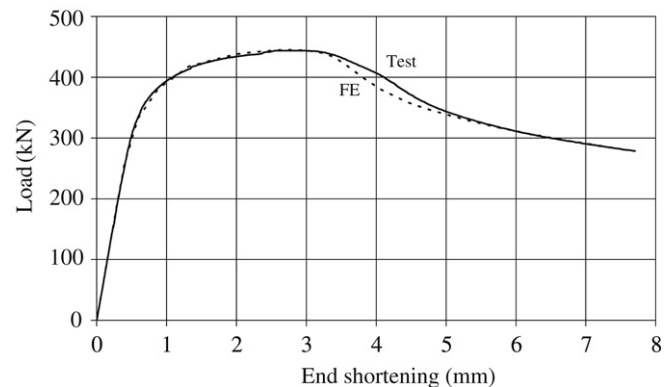
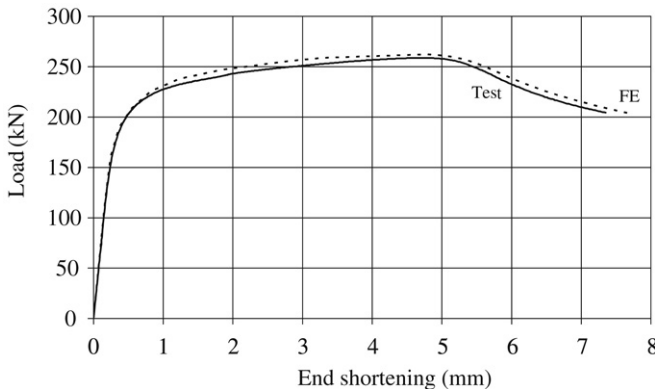


Fig. 13. Experimental and numerical load–end shortening curves for OHS 121 × 76 × 3-SC1.

material properties and an imperfection amplitude of  $t/100$  are compared with the respective experimental curves in Figs. 13 and 14 respectively. Comparison of the numerical failure mode of OHS 86 × 58 × 3-SC1 with the experimental one is depicted in Fig. 15.

Having demonstrated the ability of the numerical models to replicate the observed structural behaviour of stainless steel oval hollow sections, parametric studies were performed to investigate the structural response of OHS over a wider range of slendernesses and establish a suitable Class 3 limit in compression. The imperfection pattern was taken as the lowest buckling mode shape with an amplitude of  $t/100$ , while the material properties derived from the stub column tests on the two OHS 121 × 76 × 2



**Fig. 14.** Experimental and numerical load–end shortening curves for OHS86 × 58 × 3-SC1.



**Fig. 15.** Experimental and FE failure modes for OHS86 × 58 × 3-SC1.

specimens were averaged and incorporated into the FE models. The effect of aspect ratio on cross-sectional response was also investigated, by considering two aspect ratios—1.5 and 2. The aspect ratio of 1.5 coincides with the aspect ratio of the test specimens presented in Section 2.2 of the present paper, while the aspect ratio of 2 corresponds with carbon steel OHS examined elsewhere [9]. In the developed models, the larger outer diameter and length of the stub columns were fixed at 120 mm and 240 mm respectively, whereas the smaller outer diameter and thickness dimensions were varied to achieve the desired aspect ratio and slenderness values. The results of the stub column parametric studies are presented and discussed in Section 4.2.

### 3.3. Numerical modelling of flexural buckling members

Similarly to the stub column tests, numerical simulations of the OHS flexural buckling tests were also conducted. The boundary conditions imposed at the end cross-sections were similar to those applied to the stub column models allowing in-plane deformation of the cross-sections, but the columns' ends were also free to rotate about the axis of buckling. Kinematic coupling was employed to constrain both the vertical displacement of the loaded cross-section and the rotation of the end cross-sections about the axis of buckling considered.

Cross-section geometry, end restraints, loading and test failure modes were all symmetric with respect to the plane perpendicular to the axis of buckling for all tested specimens. This symmetry

**Table 10**

Comparison of column test results with FE results for varying imperfection amplitudes, a loading eccentricity of  $L/1250$  and stub column material properties.

Column designation	FE $F_u$ /Test $F_u$			
	Measured $e_0$	$L/500$	$L/1000$	$L/1500$
86 × 58 × 3-CMI1	1.02	0.96	0.99	1.00
86 × 58 × 3-CMA1	1.03	0.99	1.01	1.02
86 × 58 × 3-CMI2	0.97	0.93	1.00	1.03
86 × 58 × 3-CMA2	0.98	0.95	1.00	1.02
86 × 58 × 3-CM13	0.92	0.87	0.93	0.96
86 × 58 × 3-CMI4	1.03	0.95	1.01	1.03
Mean	0.99	0.95	0.99	1.01
COV	0.05	0.04	0.03	0.03

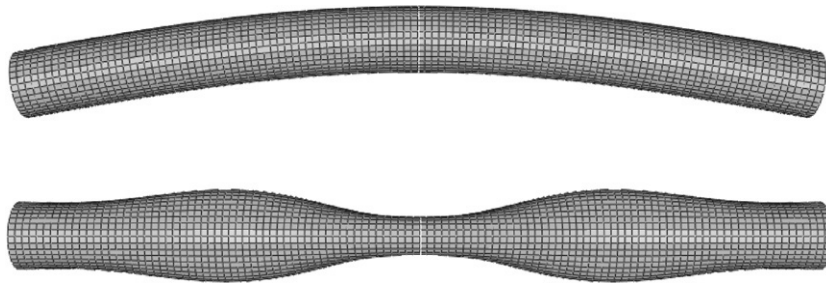
was exploited by modelling only half of the cross-section and employing symmetry boundary conditions. Furthermore, with a symmetric imperfection pattern, all FE failure modes were also symmetric with respect to the plane perpendicular to their member axis at mid-height. Hence only half the member length was modelled, thereby achieving significant reductions in computational time. This latter symmetry assumption was verified by comparing full-length with half-length models; the results were found to coincide.

Both global and local initial geometric imperfections in the form of the lowest elastic global and local buckling modes, together with the observed loading eccentricity of  $L/1250$  with respect to the axis of buckling, were incorporated into the models. Typical local and global mode shapes are shown in Fig. 16. The amplitude of the local imperfections considered was fixed at  $t/100$ , which was shown to provide accurate results for the stub column models, while the global imperfection amplitude was varied to assess the sensitivity of the model. Four global imperfection amplitudes were considered; the measured amplitude  $e$  (Table 6),  $L/500$ ,  $L/1000$  and  $L/1500$ . The influence of the local imperfection on the column response was found to be insignificant for the range of member slendernesses considered; the response of the models was dominated by the global imperfection amplitude, with no evidence of significant mode interaction.

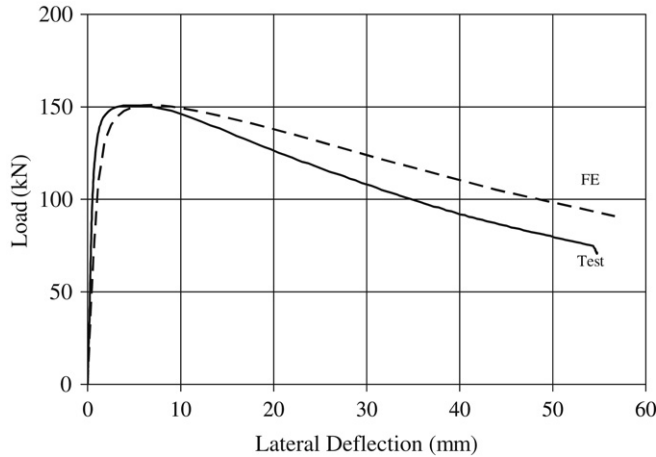
For material properties and residual stresses, the same assumptions made for the stub column models were also adopted for the long column models. Both tensile coupon and stub column properties were incorporated into the FE models for each considered imperfection amplitude. Although accurate replication of tests ultimate loads could be obtained for both cases, provided that a suitable global imperfection amplitude was chosen, the stub column properties were found to give more consistent results and were able to mimic more accurately the overall load–lateral deflection response. For this reason, the stub column material properties were used in all subsequent FE models.

Table 10 presents the ratios of numerical to experimental ultimate loads for the case of stub column material properties, a local imperfection amplitude of  $t/100$  and various global imperfection amplitudes. For a global imperfection amplitude of  $L/1000$ , an average value of numerical over experimental ultimate load of 0.99 with a corresponding coefficient of variation of 0.03 was obtained. Figs. 17 and 18 depict comparisons between numerical and experimental load–lateral deflection curves for column specimens CMA2 and CMI4 respectively.

Having validated the numerical models against experimental results, parametric studies were carried out to investigate the behaviour of stainless steel OHS column response over a wider range of member slendernesses. Both major and minor axis buckling was studied. In the parametric studies, the non-dimensional slenderness  $\lambda$  of the columns was varied between 0.2 and 2.4 in increments of 0.2 for both axes. Two cross-section aspect ratios, 1.5 and 2, were considered for each axis of buckling.



**Fig. 16.** Typical column local and global buckling mode shapes.



**Fig. 17.** Experimental and numerical load-lateral deflection curves for CMA2.

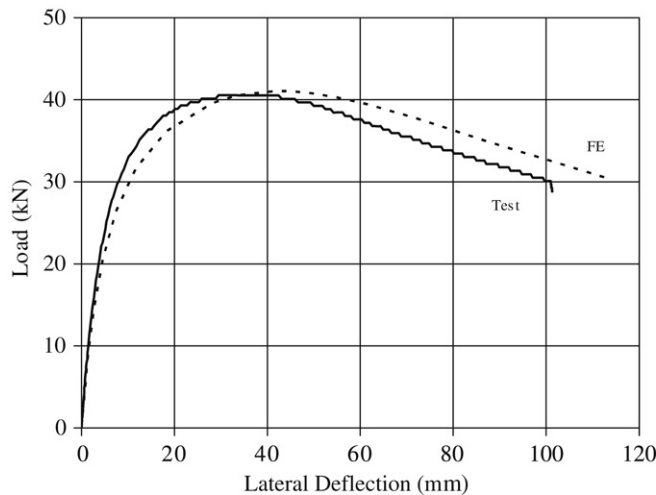


**Fig. 18.** Experimental and numerical load-lateral deflection curves for CMI4.

The modelled columns had cross-sections of  $86 \times 57.33 \times 3$  and  $86 \times 43 \times 4$  (providing aspect ratios of 1.5 and 2 respectively), with lengths varying between 224 mm and 5022 mm to achieve the desired non-dimensional slenderness values. The cross-sections considered were relatively stocky and assumed to be fully effective. The models incorporated stub column material properties (from the  $86 \times 58 \times 3$  stub columns) and included both local and global imperfections of amplitudes  $t/100$  and  $L/1000$  respectively. Loading eccentricities were not included in the parametric studies, since these were primarily related to the experimental setup and are not an inherent characteristic of the sections considered in this paper. The results are presented and discussed in Section 4.3 of this paper.

#### 4. Analysis of results and design recommendations

##### 4.1. Introduction

In this section, all test data and numerically generated results on stainless steel OHS stub columns and long columns are analysed and discussed. Comparisons are made with existing compression test data on carbon steel elliptical hollow sections (EHS) stub columns and stainless steel CHS stub columns and long columns. The applicability of current design guidance for classification and column buckling to OHS compression members is assessed and new design recommendations are proposed. It should be noted that in all code comparisons presented in this section, the measured material properties (derived from tensile coupon tests) and measured geometry have been employed.

##### 4.2. Cross-sections in compression

The codified treatment of local buckling is based on the concept of cross-section classification [4,5]. Cross-sections are assigned to discrete behavioural classes according to the effect of local buckling on their structural response. With respect to the fundamental loading case of pure compression, cross-sections capable of reaching their squash load  $F_y$  (for stainless steel defined as the cross-sectional area multiplied by the 0.2% proof stress) are characterized as fully effective (Class 1–3), whilst those that fail below  $F_y$  are characterized as slender (Class 4). Classification is made by comparing the slenderness of the cross-section with prescribed codified limits.

Due to the recent introduction of OHS in the construction industry, no specific slenderness parameter is currently defined in any code of practice for either carbon steel or stainless steel. Adoption of a suitable slenderness parameter is central to the classification process. Based on the elastic critical stress of an elliptical hollow section in pure compression, the following slenderness parameter [9,10] has been proposed for carbon steel elliptical hollow sections (EHS):

$$\frac{D_e}{t\varepsilon_{cs}^2} = 2 \frac{(a^2/b)}{t\varepsilon_{cs}^2} \quad (5)$$

where  $D_e$  is an equivalent diameter defined as two times the maximum radius of curvature in an elliptical section which is equal to  $2(a^2/b)$ ,  $E$  is Young's modulus,  $\nu$  is Poisson's ratio and  $\varepsilon_{cs} = \sqrt{235/\sigma_{0.2}}$ .

For application to stainless steel OHS, this slenderness parameter can be slightly modified by defining  $\varepsilon_{ss}$  as Eq. (6), in accordance with [4].

$$\varepsilon_{ss} = \sqrt{\frac{235}{\sigma_{0.2}} \frac{E}{210000}}. \quad (6)$$

The  $F_u/F_y$  (ultimate load over squash load) ratio of all experimental and FE data on stainless steel OHS has been plotted against this

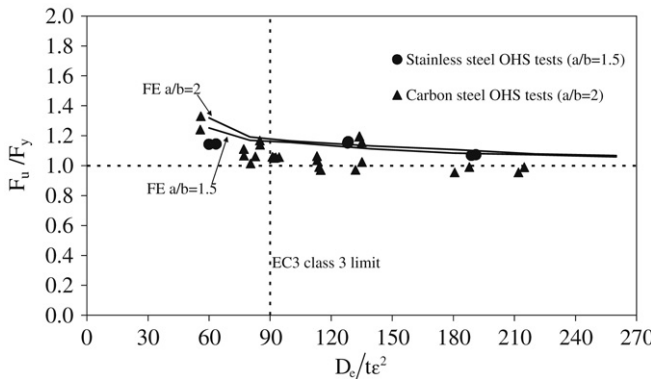


**Fig. 19.** Comparison between carbon steel and stainless steel OHS test results and FE results.

cross-section slenderness parameter in Fig. 19. For comparison purposes, existing experimental data on carbon steel EHS stub columns [9] have been added to Fig. 19; their slenderness parameter is based on \$\varepsilon\_{cs}\$. The current Eurocode 3 slenderness limit of 90 for carbon steel [5] and stainless steel [4] CHS in pure compression are also depicted. Cross-sections with a \$F\_u/F\_y\$ ratio greater than unity are capable of reaching their squash load and are therefore fully effective (Class 1–3), whilst the remaining cross-sections are prone to local buckling prior to the attainment of their squash load and are therefore characterized as slender (Class 4).

The parametric studies indicate that the OHS with the higher aspect ratio (2.0) exhibit superior load-carrying capacities to those with the lower aspect ratio (1.5) in the stocky range of the graph. This enhanced performance may be attributed to the stiffer corner regions (with low radius of curvature), which provide restraint to the less stiff flatter regions of the OHS (with high radius of curvature) and allow for greater strains and thus strain-hardening to be achieved before the ultimate load-carrying capacity of the cross-section is reached.

A more sophisticated slenderness parameter, based on a more precise evaluation of the elastic buckling stress of an elliptical tube [32] following extensive analytical and numerical studies, is given by Eq. (7).

$$D_{Eq,OHS} = \frac{2a}{te_{ss}^2} \left( 1 + f \left( \frac{a}{b} - 1 \right) \right) \quad (7)$$

where \$D\_{Eq,OHS}\$ is the equivalent OHS diameter to be used in place of \$D\_e\$ in Eq. (5) and \$f\$ is given by Eq. (8), derived from numerical results.

$$f = 1 - 2.3 \left( \frac{t}{2a} \right)^{0.6} \quad (8)$$

The equivalent diameter referred to in Eq. (7) is also limited by a plate bound in [32], but this only governs for stocky sections of high aspect ratio, not considered in the present study.

Using this more precise expression as the OHS slenderness parameter, the variation in response between high and low aspect ratio OHS is clearly reduced, as can be seen in Fig. 20. For comparison, stainless steel CHS test results [30,33–37] have also been included in Fig. 20. All CHS and OHS data follow a similar trend, throughout the full slenderness range considered, regardless of aspect ratio. Thus, the slenderness parameter given by Eq. (7) [32] is more complex than that of Eq. (5), but provides a better representation of the behaviour of stainless steel OHS over a range of aspect ratios.

From both Figs. 19 and 20, it can be seen that load-carrying capacity (normalised by squash load) decreases with increasing slenderness for both experimental CHS and OHS and numerical

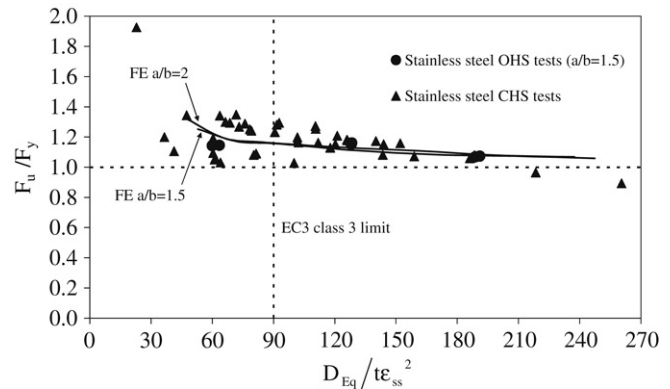


**Fig. 20.** Comparison between stainless steel OHS and CHS test results and FE results.

stainless steel OHS data. The stainless steel OHS may generally be seen to exhibit superior load-carrying in comparison to their carbon steel counterparts, since most of the carbon steel EHS test results (all having an aspect ratio of 2) lie below the corresponding stainless steel curve, as shown in Fig. 19. Hence the current Class 3 slenderness limit of 90 given in Eurocode 3 for (carbon steel and stainless steel) CHS in pure compression may be safely applied to stainless steel OHS in compression.

#### 4.3. Flexural buckling

Current European codified provisions for column buckling are based on the classic Ayrton-Perry [38] approach, originally derived for carbon steel columns, the underlying principle of which is that the loss of stiffness due to material yielding of the most heavily stressed fibre of the column triggers member instability. Although less clearly applicable to stainless steel columns due to the rounded nature of the material stress-strain curve, the same cross-sectional failure criterion is adopted, which, upon mathematical manipulation, results in the familiar buckling reduction factor formulae [4,5] given by Eq. (9):

$$\chi = \frac{1}{\Phi + (\Phi^2 - \lambda^2)^{0.5}} \leq 1 \quad (9)$$

where \$\Phi = 0.5(1 + \alpha(\bar{\lambda} - \bar{\lambda}\_0) + \bar{\lambda}^2)\$, in which \$\alpha\$ is an imperfection factor, \$\bar{\lambda}\_0\$ is the limiting slenderness, below which member buckling effects may be neglected and \$\bar{\lambda}\$ is the member slenderness defined by Eq. (2).

Column buckling resistance is determined by multiplying the buckling reduction factor \$\chi\$ by the corresponding cross-section resistance. The imperfection factor \$\alpha\$ and the limiting slenderness \$\bar{\lambda}\_0\$ allow for the influence of imperfections (principally geometric imperfections and residual stresses) on buckling resistance and depend on cross-section type, axis of buckling and forming process. It is reasonable to assume that all cold-formed hollow sections will display similar residual stresses and geometric imperfections patterns, because of similar production process. Hence the buckling curve specified in EN 1993-1-4 [4] for stainless steel SHS, RHS and CHS, which is defined by \$\alpha = 0.49\$, \$\bar{\lambda}\_0 = 0.4\$, would also be expected to be applicable to stainless steel OHS.

For comparison with codified buckling curves, the ultimate loads attained in stainless steel OHS column tests, normalised by their corresponding squash loads, have been plotted against the member slenderness (as reported in Table 7) in Fig. 21. The codified buckling curve currently applied to stainless steel SHS, RHS and CHS is also depicted. Test data on stainless steel CHS columns and stub columns [30,33–37] as well as OHS stub columns (Section 2.3) have also been included in Fig. 21 for comparison. With the

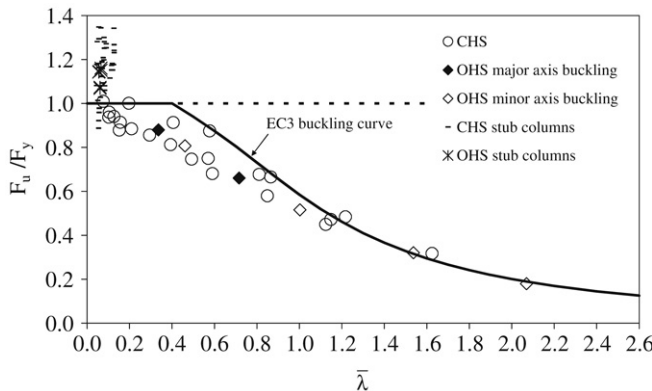


**Fig. 21.** Normalised OHS and CHS test results and column buckling curves.

exception of the very stocky members (i.e. stub columns), almost all test points lie below the current buckling curve. Hence, the current codified buckling curve is deemed unsafe for stainless steel CHS and OHS, particularly in the low and intermediate slenderness range and adoption of a revised buckling curve for CHS and OHS columns is necessary to ensure reliable design.

The shortcomings of the current provisions [4] for CHS column buckling have been previously highlighted by other researchers [39] and attributed to the fact that the calibration of the EN 1993-1-4 strength curve was based primarily on tests of cold-formed SHS and RHS columns for which substantial increases in strength is derived from the highly cold-worked corner regions. Ellobody and Young [40], following on an extensive finite element investigation, proposed two different buckling curves for stainless steel CHS columns, differentiated by material grade. These proposed curves offer improved fit to available data, but the minimum limiting slenderness  $\bar{\lambda}_0$  of 0.2 appears unconservative in the light of the presented test results (see Fig. 21). Ashraf et al. [41] also recognised this deficiency in the current provisions for stainless steel CHS columns and proposed a new buckling curve defined by a limiting slenderness value  $\bar{\lambda}_0$  of 0.05 and an imperfection factor  $\alpha$  of 0.49, which is found to be in good agreement with both the test data and the numerical results obtained from the OHS column parametric studies, as can be seen in Fig. 22. The proposed buckling curve has been statistically validated according to Annex D of EN 1990 [42] against all available CHS and OHS column test results and was deemed safe for design in conjunction with a partial safety factor of  $\gamma_{M1} = 1.1$  as specified in EN 1993-1-4 [4]. Adoption of this curve ( $\bar{\lambda}_0 = 0.49$  and  $\alpha = 0.05$ ) for both CHS and OHS column buckling is therefore proposed in the current paper.

## 5. Conclusions

Experimental and numerical structural performance data for stainless steel OHS compression members have been generated. Six OHS stub columns and six OHS long columns were tested in axial compression. These member tests were supplemented by tensile coupon tests on material cut from the cold-formed cross-sections. FE models were developed and validated against the tests. Subsequent parametric studies enabled investigation of the compressive response of OHS over a wider range of slendernesses and aspect ratios. With respect to the cross-sectional response of OHS in compression, two proposed local slenderness parameters, originally derived for carbon steel EHS, were assessed and found to be applicable for design purposes to stainless steel OHS; one being simple and more conservative, the other being more elaborate and accurate. Moreover, it was concluded that the current Class

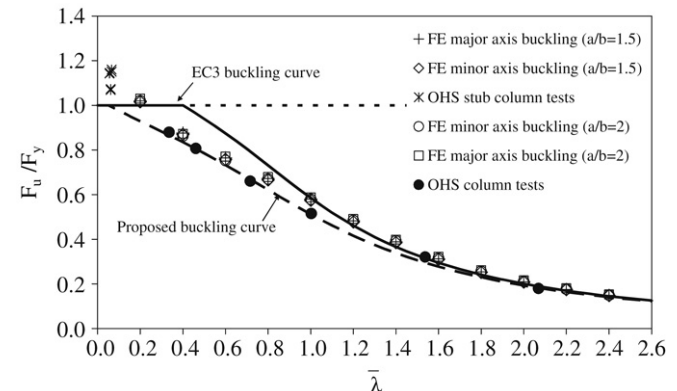


**Fig. 22.** Normalised test and FE OHS results and column buckling curves.

3 slenderness limit of 90 applied in Eurocode 3 to both carbon steel and stainless steel CHS in pure compression may be safely used for stainless steel OHS. Finally, the current codified buckling curve for stainless steel hollow sections [4] was assessed and was found inappropriate (unsafe) for both OHS and CHS. A new buckling curve [41] for CHS with a limiting slenderness value  $\bar{\lambda}_0$  of 0.05 and an imperfection factor  $\alpha$  of 0.49 was found to be in excellent agreement with both experimental and numerical test results on OHS columns buckling about either axis, and its adoption for stainless steel OHS and CHS columns is proposed in the present paper.

## Acknowledgements

The authors are grateful to Oval 316 for the supply of test specimens and technical data, and would like to thank Gemma Aubeeluck and Namrata Ghelani for their contributions to this research.

## References

- [1] Gardner L. The use of stainless steel in structures. *Prog Struct Eng Mater* 2005; 7(2):45–55.
- [2] Gardner L, Baddoo NR. Fire testing and design of stainless steel structures. *J Construct Steel Res* 2006;62(6):532–43.
- [3] Gardner L. Stainless steel structures in fire. *Proc Institut Civil Eng—Struct Buildings* 2007;160(3):129–38.
- [4] EN 1993-1-4. Eurocode 3: Design of steel structures—Part 1.4: General rules—Supplementary rules for stainless steel. CEN; 2006.
- [5] EN 1993-1-1. Eurocode 3: Design of steel structures—Part 1.1: General rules—General rules and rules for buildings. CEN; 2005.
- [6] Ashraf M, Gardner L, Nethercot DA. Structural stainless steel design: Resistance based on deformation capacity. *J Struct Eng, ASCE*. 2008;134(3):402–11.
- [7] Gardner L, Ashraf M. Structural design for non-linear metallic materials. *Eng Struct* 2006;28(6):926–34.
- [8] Baddoo NR, Burgan R, Ogden R. Architects' guide to stainless steel. SCI-P-179. UK: The Steel Construction Institute; 1997.
- [9] Chan TM, Gardner L. Compressive resistance of hot-rolled elliptical hollow sections. *Eng Struct* 2007;30(2):522–32.
- [10] Gardner L, Chan TM. Cross-section classification of elliptical hollow sections. *Steel Composite Struct* 2007;7(3):185–200.
- [11] Chan TM, Gardner L. Flexural buckling of elliptical hollow section columns. *J Struct Eng, ASCE*. [in press].
- [12] EN 10088-1. Stainless steels—Part 1: List of stainless steels. CEN; 2005.
- [13] EN 10088-2. Stainless steels—Part 2: Technical delivery conditions for sheet/plate and strip of corrosion resisting steels for general purposes. CEN; 2005.
- [14] Talja A, Salmi P. Design of stainless steel RHS beams, columns and beam-columns. Research note 1619. VTT building technology, Finland; 1995.
- [15] Young B, Lui Y. Experimental investigation of cold-formed stainless steel columns. *J Struct Eng, ASCE*. 2003;129(2):169–76.
- [16] Gardner L, Nethercot DA. Experiments on stainless steel hollow sections—Part 1: Material and cross-sectional behaviour. *J Construct Steel Res* 2004;60(9):1291–318.
- [17] Gardner L, Talja A, Baddoo NR. Structural design of high-strength austenitic stainless steel. *Thin-Walled Structures* 2006;44(5):517–28.

- [18] EN 10002-1. Metallic materials – Tensile testing – Part 1: Method of test at ambient temperature, CEN; 2001.
- [19] Mirambell E, Real E. On the calculation of deflections in structural stainless steel beams: An experimental and numerical investigation. *J Construct Steel Res* 2000;54(1):109–33.
- [20] Rasmussen KJR. Full-range stress-strain curves for stainless steel alloys. *J Construct Steel Res* 2003;59(1):47–61.
- [21] Ramberg W, Osgood WR. Description of stress-strain curves by three parameters. Technical note no 902. Washington, DC: National Advisory Committee for Aeronautics; 1943.
- [22] Hill HN. Determination of stress-strain relations from the offset yield strength values. Technical note no 927. Washington, DC: National Advisory Committee for Aeronautics; 1944.
- [23] Schafer BW, Peköz T. Computational modelling of cold-formed steel: Characterizing geometric imperfections and residual stresses. *J Construct Steel Res* 1998;47(3):193–210.
- [24] Cruise RB, Gardner L. Measurement and prediction of geometric imperfections in structural stainless steel members. *Struct Eng Mech* 2006;24(1):63–89.
- [25] ABAQUS. ABAQUS/Standard user's manual volumes I-III and ABAQUS CAE manual. Version 6.6. (Pawtucket, USA): Hibbit, Karlsson & Sorensen, Inc; 2006.
- [26] Ashraf M, Gardner L, Nethercot DA. Finite element modelling of structural stainless steel cross-sections. *Thin-walled Struct* 2006;44:1048–62.
- [27] Ellobody E, Young B. Structural performance of cold-formed high strength stainless steel columns. *J Construct Steel Res* 2005;61(12):1631–49.
- [28] Lecce M, Rasmussen KJR. Distortional buckling of cold-formed stainless steel sections: Finite-element modelling and design. *J Struct Eng, ASCE*. 2006; 132(4):505–14.
- [29] Koltsakis EK, Preftitsi FG. Numerical investigation of the plastic behaviour of short welded aluminium double-T beams. *Eng Struct* 2008;30(7):2022–31.
- [30] Rasmussen KJR, Hancock GJ. Design of cold-formed stainless steel tubular members. I: Columns.. *J Struct Eng, ASCE* 1993;119(8):2349–67.
- [31] Cruise RB, Gardner L. Residual stress analysis of structural stainless steel sections. *J Construct Steel Res* 2008;64(3):352–66.
- [32] Ruiz-Teran AM, Gardner L. Elastic buckling of elliptical tubes. *Thin-walled Struct* 2008;46(11):1304–18.
- [33] Burgan BA, Baddoo NR, Gilsenan KA. Structural design of stainless steel members – comparison between Eurocode 3, Part 1.4 and test results. *J Construct Steel Res* 2000;54(1):51–73.
- [34] Kuwamura H. Local buckling consideration in design of thin-walled stainless steel members. Lecture at Pusan National University, February 8th 2001.
- [35] Young B, Hartono W. Compression tests of stainless steel tubular members. *J Struct Eng, ASCE*. 2002;128(6):754–61.
- [36] Bardi FC, Kyriakides S. Plastic buckling of circular tubes under axial compression—part I: Experiments. *Internat J Mech Sci* 2006;48(8):830–41.
- [37] Lam D, Gardner L. Structural design of stainless steel concrete filled columns. *J Construct Steel Res* 2008;64(11):1275–82.
- [38] Ayrton WE, Perry J. On struts. *The Engineer* 1886;62:464–5.
- [39] Rasmussen KJR, Rondal J. Column curves for stainless steel alloys. *J Construct Steel Res* 2000;54(1):89–107.
- [40] Ellobody E, Young B. Investigation of cold-formed stainless steel non-slender circular hollow section columns. *Steel Composite Struct* 2007;7(4):321–37.
- [41] Ashraf M, Gardner L, Nethercot DA. Resistance of stainless steel CHS columns based on cross-section deformation capacity. *J Construct Steel Res* 2008;64(9): 962–70.
- [42] EN 1990. Eurocode—Basis of structural design. CEN; 2002.